

Bayesian Algorithm for Microwave-Based Precipitation Retrieval: Description and Application to TMI Measurements Over Ocean

Sabatino Di Michele, Alessandra Tassa, Alberto Mugnai, Frank Silvio Marzano, *Senior Member, IEEE*, Peter Bauer, and José Pedro V. Poiares Baptista

Abstract—A physically oriented inversion algorithm to retrieve precipitation from satellite-based passive microwave measurements named the Bayesian algorithm for microwave-based precipitation retrieval (BAMPR) is proposed. First, we illustrate the procedure that BAMPR follows to produce precipitation estimates from observed multichannel brightness temperatures. Retrieval products are the surface rain rates, columnar equivalent water contents, and hydrometeor content profiles, together with the associated estimation uncertainties. Numerical tests performed on simulated measurements show that retrieval errors are reduced when a rain type and pattern classification procedure is employed, and that estimates are quite sensitive to the adopted error model. Finally, for different tropical storms that were observed by the Tropical Rainfall Measuring Mission (TRMM) Microwave Imager (TMI), we compare the rain retrieved from BAMPR relative to those retrieved from the Goddard Profiling (Gprof) algorithm and the Precipitation Radar-adjusted TMI estimation of rainfall (PATER) algorithm. Despite a similar inversion approach, the algorithms exhibit different performances that can be mainly related to different training databases and retrieval constraints such as cloud classification.

Index Terms—Atmospheric remote sensing, spaceborne microwave radiometry, precipitation retrieval.

I. INTRODUCTION

A PART from its key role in the water cycle budget, the knowledge of rainfall on a global scale is important in many areas of atmospheric science. Retrieval of precipitation from spaceborne microwave sensors has reached a new dimension with the launch of the Tropical Rainfall Measuring Mission (TRMM) platform in 1997 [1]. The increased ground resolution,

Manuscript received May 19, 2004; revised November 3, 2004. This work was supported in part by the European Space Agency, in part by the Italian Space Agency, in part by the Italian National Group for Prevention from Hydrological Hazards (GNDCI), and in part by the European Commission through the EURAINSAT Project (2001–2003). S. Di Michele performed this work while at the Istituto di Scienze dell'Atmosfera e del Clima (ISAC), Consiglio Nazionale delle Ricerche (CNR), 00133 Rome, Italy

S. Di Michele and P. Bauer are with the European Centre for Medium-range Weather Forecasts (ECMWF), RG2 9AX, Reading, U.K. (e-mail: Sabatino.Di.Michele@ecmwf.int).

A. Tassa and A. Mugnai are with the Istituto di Scienze dell'Atmosfera e del Clima (ISAC), Consiglio Nazionale delle Ricerche (CNR), Via del Fosso del Cavaliere 100, 00133 Rome, Italy.

F. S. Marzano is with the Dipartimento di Ingegneria Elettrica, Centro di Eccellenza CETEMPS, Università dell'Aquila, 67040 L'Aquila, Italy.

J. P. V. P. Baptista is with the European Space Agency Space Technology Centre (ESTEC), 2200 AG Noordwijk, The Netherlands.

Digital Object Identifier 10.1109/TGRS.2005.844726

the additional 10-GHz channels of the TRMM Microwave Imager (TMI), together with the presence of the first spaceborne Precipitation Radar (PR), are characteristics designed to improve rainfall estimates.

Several inversion techniques have been proposed and applied in the last decade for estimating precipitation profiles. In particular, Bayesian techniques have been proved to have a large potential and flexibility [2]–[5]. As opposed to empirical methods where measurements of both brightness temperatures (TBs) and precipitation parameters are collected to set up a retrieval algorithm, the model-based approaches apply refined physical models to simulate the measurements [6]. This point of view offers the possibility to explicitly take into account the involved physical processes, and therefore to deepen the understanding of the forward problem. On the other hand, model-based approaches have to tackle the critical issue of tuning simulations to the measurement manifolds in order to be representative of global observations [7], [8].

This paper is a further investigation of the Bayesian algorithm for microwave-based precipitation retrieval (BAMPR) developed by many of the authors and first described in [9]. This algorithm has been first developed for using data acquired by the TMI over ocean. A combined version—for active and passive sensor merging—aims at the exploitation of data from the PR aboard the TRMM platform [10], while the extension to land surface is under development.

Aim of the work is the discussion of some new features introduced in BAMPR to tackle some specific issues inherent to the retrieval of precipitation from space using passive microwave sensors. In particular, we illustrate the impact of a rain-type and pattern classification procedure on the final estimates. Also, we show that estimation results are very sensitive to the assumptions made for the modeling errors.

The paper is organized as follows. First, a general description of the inversion methodology is given in Section II. Then, results of numerical tests on synthetic measurements are shown in Section III. Finally, BAMPR rain estimates are compared with the ones of two other referenced algorithms for TMI and with the standard rain product from the TRMM PR in Section IV.

II. FEATURES OF THE RETRIEVAL METHODOLOGY

A. Retrieval Scheme for the Inverse Problem

The inversion scheme implemented in BAMPR is outlined by the block-diagram in Fig. 1. The cloud-radiation database

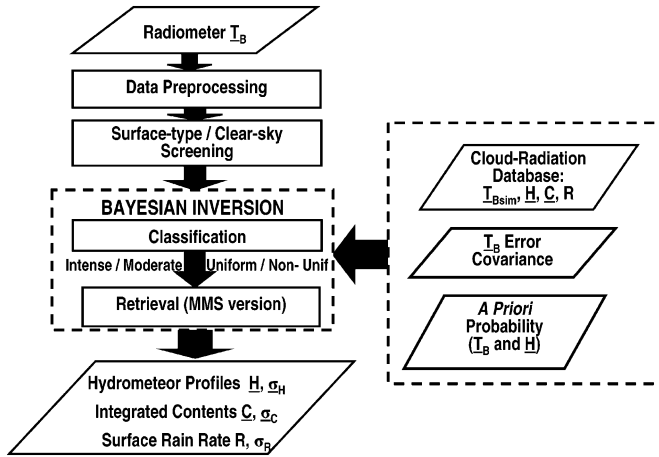


Fig. 1. Scheme of BAMPR.

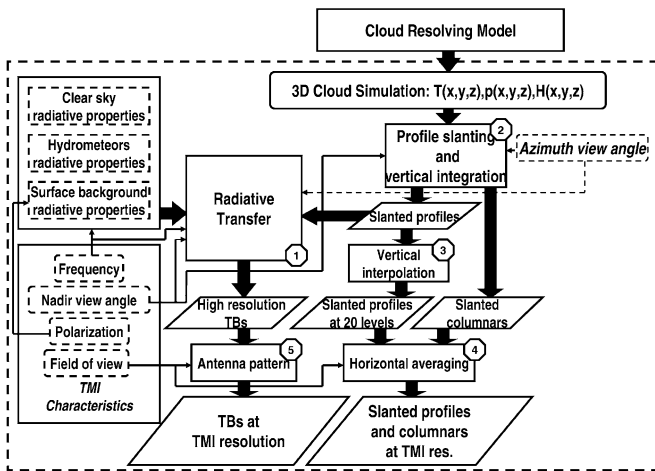


Fig. 2. Scheme of the cloud-radiation database generation for BAMPR.

(CRD) consists of a large set (several thousands) of slanted precipitating cloud profiles and of the corresponding brightness temperatures (TBs) at TMI channels and resolutions [9]. The CRD is also characterized by its error covariance matrix, that summarizes all the errors and uncertainties intrinsic to the CRD generation as described in [11]. Cloud simulations from four different mesoscale cloud resolving model (CRM) have been used to build the BAMPR tropical CRD: the University of Wisconsin Non-Hydrostatic Modeling System (UW-NMS) [12], the Goddard Cumulus Ensemble Model (GCE) [13], the Méso-NH (MESONH) [14], and the JCMM model [15]. All of them describe the temporal and spatial patterns of given meteorological events, but also the three-dimensional (3-D) structures of the meteorological variables (air temperature, pressure, and humidity) and the liquid/ice water contents of six different types of hydrometeors (four frozen and two liquid species).

A global view of the process for generating the CRD is given by the flow-chart in Fig. 2. TBs are computed by means of a slanted-path, plane parallel radiative transfer (RT) scheme [16]–[18]. The polarization information is used only for computing the surface characteristics, because all hydrometeors are modeled as spheres following Mie theory. In the RT module

TABLE I
COMPOSITION OF THE TMI TROPICAL CRD USED IN BAMPR

Model	Cloud System	Grid Resol. (km)	Minutes	Azimuth	Ocean Wind Speed (m/sec)	Nr. of files	Nr. of profiles per file	Total nr. of profiles
UW-NMS/HC-3	Hurricane Gilbert	2.5	3100, 3530	0, 90, 180, 270	10., 20.	16	24x38	14592
UW-NMS/HC-3	Hurricane Bonnie	3.3	2130, 2340	0, 90, 180, 270	5., 10., 20. (for 2130) 20 (for 2340)	16	82x92	120704
GCE/TC-1	Squall Line TOGA-COARE	1.0	180, 240	0, 90, 180, 270	10., 20.	16	34x69	37536
Méso-NH/TC-1	Squall Line TOGA-COARE	1.25	300, 360, 420, 480	0., 180.	5., 10., 20.	24	17x139	56712
JCMM/TC-1	Squall Line TOGA-COARE	1.25	270, 360	0, 90, 180, 270	5., 10., 20.	24	49x65	67080
Total								296,624

(block nr. 1 in the picture), Marshall-Palmer drop-size distributions with constant slopes (UW-NMS) or constant intercepts (GCE, MESO-NH and JCMM) have been used. The TBs are computed at model resolution and eventually averaged to sensor resolution through a Gaussian-shaped weighting function (block nr. 5). The associated profiles are slanted and vertically (linearly) interpolated to 20 levels as well as averaged at the resolution of the TMI 37-GHz channel. The RT model has been applied to each of the available 3-D clouds that are output of the different CRMs, imposing various ocean wind speeds to account for variable surface conditions. RT calculations have been repeated at four complementary observational azimuth angles, since the effect of azimuth angle at which the cloud is observed is relevant. Table I gives details of the composition of the CRD. More details about the CRD generation can be found in [9]. Note, that the database only contains profiles from tropical systems for application to TRMM data. It therefore does not represent all possible tropical storms but rather represents their general characteristics (e.g., freezing level height, columnar content, etc.).

The CRD is used as an input to a Bayesian inversion algorithm. The estimation does not only come from a direct comparison between measured TBs and those contained in the CRD, but two additional stages are necessary. The first one is the screening phase where a rain detection scheme is applied. Land and coast pixels are removed according to their geolocation. The rain detection method is the same as that of the official TMI rain product and is based on the work of Ferraro *et al.* [19]. The second step of the retrieval algorithm defines qualitative aspects of the scene for which a rainfall estimate is made. For this purpose, the BAMPR algorithm classifies rain events into *moderate* (M) or *intense* (I) regimes and into *uniform* (U) or *nonuniform* (N) systems.

Finally, the actual rain estimation is carried out. Output products are the hydrometeor content and/or precipitation-rate profiles, columnar liquid/ice water contents (LWCs) and surface rain rates. These parameters are evaluated according to the minimum mean square (MMS) criterion. If \mathbf{g} is the vector of cloud parameters, $p(\mathbf{g})$ is their probability density function (pdf), and

\mathbf{t}_m is the measurement vector, the MMS solution $\hat{\mathbf{g}}_{\text{MMS}}$ is given by

$$\hat{\mathbf{g}}_{\text{MMS}} = \frac{1}{p(\mathbf{t}_m)(2\pi)^{p/2}\sqrt{\det(\mathbf{C}_{\varepsilon_t})}} \times \int \mathbf{g} \exp[-0.5(\varepsilon_t - \bar{\varepsilon}_t)^T \mathbf{C}_{\varepsilon_t}^{-1}(\varepsilon_t - \bar{\varepsilon}_t)] p(\mathbf{g}) d\mathbf{g} \quad (1)$$

where $\varepsilon_t(\mathbf{g}) = \mathbf{t}_m - \mathbf{t}(\mathbf{g})$ is the departure of the measured TBs from the ones associated with cloud profile \mathbf{g} according to the employed RT model. $\bar{\varepsilon}_t$ and $\mathbf{C}_{\varepsilon_t}$ denote the mean value and the covariance matrix of ε_t , respectively. The integration in (1) is applied only to the corresponding portion of the CRD, that is within each of the above defined rain classes.

The quantification of retrieval accuracy, $\sigma_{\hat{\mathbf{g}}_{\text{MMS}}}^2$, is similarly important as the estimate itself. For example, satellite rainfall estimates can be assimilated into numerical weather prediction models only if the corresponding accuracies are provided [20]. With the hypothesis that the components of \mathbf{g} are uncorrelated, the uncertainty can be expressed as

$$\sigma_{\hat{\mathbf{g}}_{\text{MMS}}}^2 = \frac{1}{p(\mathbf{t}_m)(2\pi)^{p/2}\sqrt{\det(\mathbf{C}_{\varepsilon_t})}} \times \int \mathbf{g}^2 \exp[-0.5(\varepsilon_t - \bar{\varepsilon}_t)^T \mathbf{C}_{\varepsilon_t}^{-1}(\varepsilon_t - \bar{\varepsilon}_t)] p(\mathbf{g}) d\mathbf{g} - \hat{\mathbf{g}}_{\text{MMS}}^2. \quad (2)$$

The derivation of the previous formulae is given in Appendix I as well as a general discussion about the Bayesian approach. A description of the numerical implementation of (1) and (2) can be found in [9].

B. Description of the Classification Procedure

Prior to the estimation, BAMPR has a classification step. Each pixel of the observed scene is flagged as *moderate* or *intense*, *uniform*, or *nonuniform* to give a first qualitative description of the rain regime and of its pattern. This procedure is intended to mitigate the ill-conditioning of the problem, since it focuses the retrieval on the most appropriate portion of the CRD (and is also useful for speeding up the retrieval). As a matter of fact, the ensemble of all profiles/TBs contained in the CRD does not constitute a functional relationship, since different profiles (with different rain intensities) may produce the same vector of TBs. This is partly due to the saturation in the emission and partly due to the effect of the spatial resolution (partial beam filling). The classification aims at defining a more “functional” TB/rain relationship considering only those profiles for the estimates that have a rain content and a spatial TB-structure that resemble the ones identified for the measurements. Although a possible misclassification could deteriorate the retrieval, benefits brought by a more proper use of the CRD largely exceed this drawback.

Uniform/Nonuniform: The U-N discrimination aims at considering only those CRD profiles characterized by spatial TB features similar to the ones of the observed TBs. To give a measure of the homogeneity of the structure, an analysis of the spatial structure of the measured TMI TBs at 37 and 85 GHz is performed. These TMI frequencies have been chosen because they have the highest spatial resolution (i.e., 13 and 5 km, respectively) that is similar to the typical rain cells dimension (about 5–10 km) [21].

It is important to point out that this kind of classification does not represent a definition of the subpixel variability. Although very important [22], [23], this issue goes beyond the purpose of our technique. On the contrary, in the context of the BAMPR algorithm, we are interested in an optimal use of the lower resolution channels using spatial information from the higher resolution channels.

The use of texture variables to classify the scene under observation is well established in the case of visible/infrared radiometric measurements because of their high spatial resolution [24]. The improvement in resolution of TMI with respect to previous microwave radiometers such as Special Sensor Microwave Imagers (SSM/I) allows the exploitation of spatial pattern also for microwaves. Various studies have already demonstrated the usefulness of this type of information, e.g., in improving the distinction between stratiform and convective rain [22], [25], [26]. We introduce two quantities as indicators of the horizontal character of the scene under observation. The first one is the normalized standard deviation of the TBs in a defined spatial window. Considering the pixel (i, j) , and the matrix composed of the surrounding $(2m + 1)$ by $(2m + 1)$ pixel pattern, it can be written as

$$S(i, j, m) = \frac{1}{\bar{t}} \sqrt{\frac{1}{(2m)^2} \sum_{i'=-m, i' \neq 0}^m \sum_{j'=-m, j' \neq 0}^m (t(i', j') - \bar{t})^2} \quad (3)$$

where \bar{t} is the average TB in the matrix.

The second parameter is the average TB gradient, defined as the mean difference between the center-pixel TB and the TBs at distance m

$$G(i, j, m) = \frac{1}{t(i, j)} \left(\frac{1}{4(2m+1)} \sum_{\text{ring}(m)} (t(i', j') - t(i, j)) \right). \quad (4)$$

These two quantities are complementary, since S gives the spatial variability in the window, and G identifies those pixels with an isolated TB enhancement or depression, thus corresponding to low standard deviation of TBs. In BAMPR, we calculate S and G from TMI TB channels at 37 and 85 GHz considering a 3×3 pixel domain ($m = 1$). This roughly corresponds to the 10-GHz channel footprint size [27].

In this way, the proposed quantities can be seen as indirect indicators of the beam filling within the 10- and 19-GHz footprints. It is noteworthy that while G is calculated for both frequencies, S is only computed for the TBs at 85 GHz. This is because S at 37 GHz only resolves large-scale cloud borders but not storm-scale features due to the insufficient spatial resolution of the TMI. The use of more sophisticated pattern variables to better define the spatial structures is related to the ability of cloud resolving models in reproducing the spatial features of real events at a finer grid [28].

The definition of each pixel as U or N is based upon the values of S and G , fixing threshold values ($G_{37v,th}$, $G_{85v,th}$, $S_{85v,th}$). If at least one of G or S is below the threshold, the pixel under observation is flagged as N. The thresholds (given in Table II) have been derived evaluating G_{37v} , G_{85v} , and S_{85v} from TB maps of different CRM simulations. Their values are the ones

TABLE II
PATTERN INDICATOR THRESHOLDS USED TO DISTINGUISH BETWEEN
UNIFORM AND NONUNIFORM PIXELS

	G_{37v}	G_{37h}	G_{85v}	G_{85h}	S_{85v}	S_{85h}
Non Uniform if greater than this	0.15	0.15	0.2	0.2	0.15	0.15
Non Uniform if lower than this	-0.15	-0.15	-0.2	-0.2	n.a.	n.a.

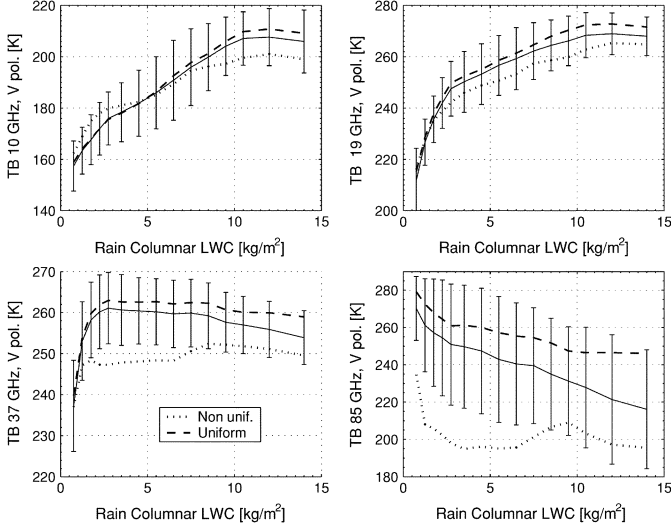


Fig. 3. Mean relationships between rain columnar content and corresponding simulated TB at (upper left panel) 10 GHz, (upper right panel) 19 GHz, (lower right panel) 37 GHz, and (lower left panel) 85 GHz. Black curves are for the whole BAMPR CRD (error bars represent the standard deviation), while dashed and dotted curves are, respectively, for the portions identified as uniform or nonuniform by the classification.

found to best identify inhomogeneous profiles (in a statistical sense). In case of TRMM, a multisensor approach could be implemented to define $G_{37v,th}$, $G_{85v,th}$, $S_{85v,th}$ exploiting PR-derived rain pattern information with matched G_{37v} , G_{85v} , and S_{85v} derived from coincident TMI and VIRS TBs.

Fig. 3 shows the average TB/rain relationships for the whole BAMPR CRD and separately for the U and N classes (defined as above). As expected, the N class is characterized by very low 85-GHz TBs. At 10, 19, and 37 GHz, the N profiles tend to have lower TBs than the U ones which is a consequence of the nonuniform beam filling effect [29]. However we note that this characteristic is reversed at 10 GHz for columnar rain contents lower than about 5 kg/m². This is because rain is given at the resolution of the 37-GHz channel (i.e., the BAMPR product resolution) so that the TB–rain relationship is poorly represented due to the very coarse resolution of the 10-GHz channel.

Moderate/Intense: Beside the U-N classification, each pixel is also classified as M or I. The two regimes are classified according to the columnar rain LWC at the TMI 37-GHz channels resolution (i.e., 15 × 10 km²) which is the one of BAMPR products. The distinction between M and I is made choosing a rain LWC threshold of 3.5 kg/m² that roughly corresponds to 15 mm/h of surface precipitation. For this value, TBs at 19 GHz become saturated. Sensitivity tests (not shown) suggested that

TABLE III
TB CENTROIDS USED TO IDENTIFY EACH CLASS. VALUES RELATIVE TO
MODERATE/INTENSE SEPARATION AND TO A UNIFORM/NONUNIFORM
PLUS MODERATE/INTENSE ARE GIVEN

	TB 10 GHz, V pol.	TB 10GHz, H pol.	TB 19 GHz, V pol.	TB 19 GHz, H pol.	TB 37 GHz, V pol.	TB 37 GHz, H pol.	TB 85 GHz, V pol.	TB 85 GHz, H pol.
M	194	135	244	217	255	239	261	259
I	225	187	270	264	256	255	229	229
UM	195	135	245	217	256	240	262	260
NM	193	134	242	215	239	225	209	208
UI	224	185	271	264	258	257	236	236
NI	234	200	269	262	236	235	175	175

this value represents the one that maximizes the probability of correct class detection. First, centroids for M and I classes are calculated (as mean TBs) separating the whole CRD according to the rain LWC. Then, two sets of centroids are derived repeating the operation separately for U and N pixels of the CRD.

Table III contains the obtained centroids for each of the two procedures. We recognize that a *stratiform/convective* classification (e.g., see [22]) would probably be a better solution. However, we have found that such criterion is hardly applicable over slanted profiles of the adopted cloud model simulations. Moreover, a *stratiform/convective* classification is not easy to extract from the radiometric signature alone because mixed convective and stratiform portions often coexist within the same cloud structure [30] and a misleading classification could compromise the estimate.

III. TESTS ON SYNTHETIC DATA

In this section, we will describe some retrieval tests performed using BAMPR with synthetic TBs in order to evaluate the classification technique and to carry out an error budget analysis. Simulated TMI observations have been generated from Minute 2130 (from the model initialization time) of UW-NMS hurricane Bonnie simulation (occurred in August 1998).

A. M-I Unsupervised Separation

The distinction between U and N classes is fully “unsupervised” because it is directly based upon measured TBs. Differently, the M and I classes are defined using rain LWC, and therefore, it is necessary to evaluate a set of TBs *centroids* representing them. The definition of the centroids is a critical point of any unsupervised classification. In BAMPR, the U-N classification is performed prior to the M-I one to allow the use of different M and I centroids for the U and N pixels. In this subsection, we want to show that the M-I classification improves if information about the TB spatial pattern is also used for defining the M and I centroids. We set up an experiment where a subset of the Bonnie simulation has been separated to be used as synthetic measurements. We have chosen those profiles that define a grid corresponding to the TMI sampling in the spatial domain of the simulation. This selection criterion allows to plot

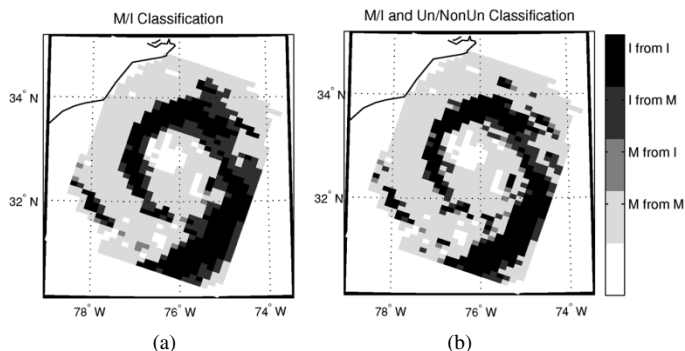


Fig. 4. Contingency maps for the moderate/intense classification. (a) Centroids are derived from a moderate/intense separation of the CRD. (b) Centroids are derived separately for uniform and nonuniform profiles of the CRD.

TABLE IV

(a) CONTINGENCY TABLE FOR MODERATE/INTENSE CLASSIFICATION USING THE CENTROIDS GIVEN IN TABLE II RELATIVE TO THE MODERATE/INTENSE SEPARATION. (b) AS IN TABLE IV(a), BUT USING CENTROIDS DERIVED SEPARATING THE TRAINING CRD BOTH AS UNIFORM/NONUNIFORM AND MODERATE/INTENSE

		True		
		<i>M</i>	<i>I</i>	Total
Estimated	<i>M</i>	56.4% (549)	1.1% (11)	57.5% (560)
	<i>I</i>	15.6% (152)	26.9% (262)	42.5% (414)
	Total	72% (701)	28% (273)	100% (974)

(a)

		True		
		<i>M</i>	<i>I</i>	Total
Estimated	<i>M</i>	62.7% (611)	2.6% (25)	65.3% (636)
	<i>I</i>	9.3% (90)	25.4% (248)	34.7% (338)
	Total	72% (701)	28% (273)	100% (974)

(b)

results of classification according to a map. Therefore, the M-I classification has been performed on those profiles. The results are summarized in Fig. 4. We note that an excess of the I class [Fig. 4(a)] is obtained when the centroids are built without considering U-N distinction. This overestimation can be attributed to the poor resolution of the channels at lower frequencies. For the same average rain value inside the field of view (FOV), an N pattern gives higher TBs than a U one. This problem can be mitigated when a preliminary separation is performed according to the spatial structure. This is shown in Fig. 4(b), where M pixels classified as I are reduced, although some I pixels seen as M still appear. Confusion matrices in Table IV show that the number of misclassified moderate pixels is reduced as well. The remaining misclassification seems to correspond to isolated rain cells having moderate intensity and extension compatible with the 10-GHz channel resolution. They are characterized by intermediate values of the 10-GHz TB, but high values for the remaining channels, and low values of the spatial variability indices. As a result, these cells cannot be properly identified, since they have the same signature of UM pixels.

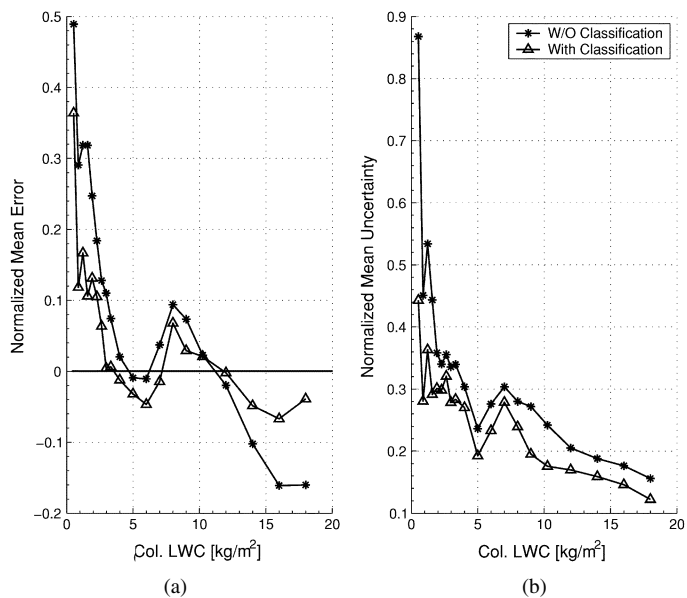


Fig. 5. Mean normalized error (left panel) and mean normalized uncertainty (right panel) of the rain columnar LWCs retrieved without classification (line with asterisk), and with classification (line with triangle) as a function of the rain columnar LWC.

B. Impact of Classification on Retrieval

In this subsection, we investigate how the estimation error modifies when a classification procedure is employed. Again, retrievals based on simulated measurements are performed. First, the CRD has been clustered into four classes according to the following categories: nonuniform and moderate (NM), uniform and moderate (UM), nonuniform and intense (NI), and uniform and intense (UI) using the unsupervised separation described in the previous section. For the purpose of the retrieval, a group of 4000 synthetic measurements has been defined from Minute 2130 of Bonnie simulation. From this group, 1000 profiles from each class were randomly extracted. A uniform sampling with respect to rain has been ensured by dividing the full dynamic range of columnar rain LWC of each class into ten intervals, each containing 100 samples. Retrieval tests have been performed, first without classification and then repeated using the classification.

Fig. 5(a) and (b) shows, respectively, the resulting rain columnar LWC estimation error and uncertainty in the two cases, as function of the true values. Generally, the plots show that both quantities are closer to zero for all rain regimes when the classification is performed. However, a moderate underestimation can be noted around 5 kg/m². This can be attributed to the MI misclassification for the values around the transition threshold between the M and I classes.

C. Error Budget Analysis

BAMPR is characterized by an estimation of the error covariance matrix associated to the modeling assumptions done for the RT calculations. As extensively described in [11], values are obtained by means of TB sensitivity tests with respect to some reference parameters (i.e., particle size distributions, sea surface emissivity, 3-D/1-D approximations, etc.). Here we want to analyze the impact that different assumptions for error covariance

TABLE V
(a) TB ERROR AUTOCOVARANCE USED FOR SYNTHETIC RETRIEVAL INDICATED BY THE TEST NUMBER. (b) TB ERROR CROSS-COVARIANCE USED FOR SYNTHETIC RETRIEVAL INDICATED BY THE TEST NUMBER

	TB 10 GHz, V pol. (K ²)	TB 10 GHz, H pol. (K ²)	TB 19 GHz, V pol. (K ²)	TB 19 GHz, H pol. (K ²)	TB 37 GHz, V pol. (K ²)	TB 37 GHz, H pol. (K ²)	TB 85 GHz, V pol. (K ²)	TB 85 GHz, H pol. (K ²)
Test 1, Test 5	1.0	1.0	1.4	2.2	2.6	2.6	6.7	6.7
Test 2, Test 6	1.0	1.0	5.3	12.9	2.6	2.6	6.7	6.7
Test 3, Test 7	1.0	1.0	1.4	2.2	2.6	2.6	42.2	42.2
Test 4, Test 8	1.0	1.0	5.3	12.9	2.6	2.6	42.2	42.2

(a)

	TB 19 GHz, V pol. (K ²)	TB 37 GHz, H pol. (K ²)	TB 37 GHz, V pol. (K ²)	TB 85 GHz, H pol. (K ²)	TB 85 GHz, V pol. (K ²)
Test 5	0.9	1.5	1.5	2.5	2.7
Test 6	2.7	4.4	4.5	7.5	2.7
Test 7	0.9	1.5	4.5	7.5	8.2
Test 8	2.7	4.4	13.5	22.4	8.2

(b)

matrix have on the estimation errors and uncertainties, respectively. For this purpose, we have performed some retrieval tests using the simulated measurements already employed for the experiments on classification. In each test, the total error $\epsilon_t(\mathbf{g})$ has been supposed additive, Gaussian, and with zero mean value, assuming a different form for the error covariance matrix $\mathbf{C}_{\epsilon t}$.

In a first group of four synthetic retrievals, the noise has been supposed uncorrelated among channels (i.e., $\mathbf{C}_{\epsilon t}$ diagonal), with the autocovariance values given in Table V(a). These values result from the sum of the modeling uncertainties and the instrument errors. The latter is supposed uncorrelated with standard deviation fixed to 1.5 K at 85 GHz and 1 K for the remaining channels. In Test 1, modeling errors for all channels have been set to 10% of the full TB range of variation. This percentage has been increased to 30% for channels at 19 GHz in Test 2 and Test 3, and again to the same value for channels at 85 GHz in Test 4. In the second group of four retrievals (Tests 5 to 8) the autocovariance values of the first four tests have been kept, but the noise has been considered fully correlated among channels, resulting in the cross-covariances given in Table V(b). As indicator of the performance in each test we have considered the *explained median absolute error* e , defined as

$$e = 1 - \frac{\text{median}[abs(\hat{r} - r)]}{\text{median}[abs(r - \text{median}(r))]} \quad (5)$$

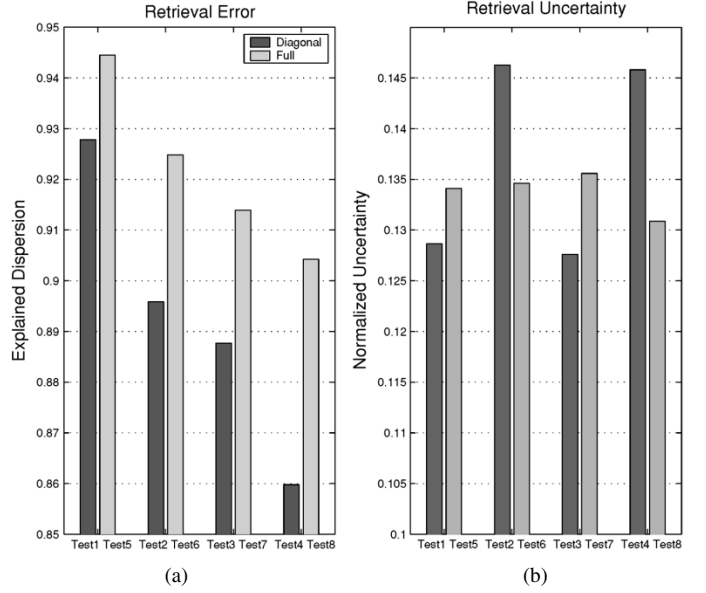


Fig. 6. (a) Estimation error and (b) uncertainty for the retrieval test having the error covariance matrices as from Table V. Dark gray bars refer to tests where off diagonal terms are set to zero, while the light gray bars correspond to when the cross-terms are also considered.

where r and \hat{r} are the true and the corresponding retrieved rain values. The choice of the median value is done to mitigate the effect of possible outliers. In addition, the estimation ambiguity is represented for each test case by means of the *mean normalized retrieval uncertainty* u , defined as

$$u = \text{mean}\left(\frac{\sigma_{\hat{r}}}{\hat{r}}\right) \quad (6)$$

where $\sigma_{\hat{r}}$ is the retrieval uncertainty evaluated according to (2). Fig. 6(a) shows e obtained for the four tests. From the analysis, it can be noted that estimation error increases with the TB-uncertainty. Comparing the estimation errors in Test 2 and Test 3, where the noise is higher for the 19 and 85 GHz, respectively, we note that the retrieval is more sensitive to noise at 85 GHz. When the interchannel correlation is considered, performances are always better. Thus, the correlation among the different components of noise could be thought as a reduction of the noise in each channel. This result puts in evidence the importance of a full description of the error covariance matrix used to describe the forward modeling errors.

As for the rain estimation uncertainty u , shown in Fig. 6(b), the maxima for Tests 2 and 4, suggest that it is more sensitive to error at 19 GHz than at 85 GHz. However, this trend is not present when the correlation among channels is introduced.

IV. APPLICATION TO TMI DATA

In the previous section, BAMPR has been applied to simulated measurements in order to investigate some issues of the adopted retrieval methodology, i.e., the classification and the modeling errors. However, real measurements are to be employed to fully understand its behavior. Thus, in this section we show the results of applying BAMPR to several TRMM cases. Resulting rain estimates are compared to the ones of two other TMI retrieval algorithms and to the ones of the TRMM PR.

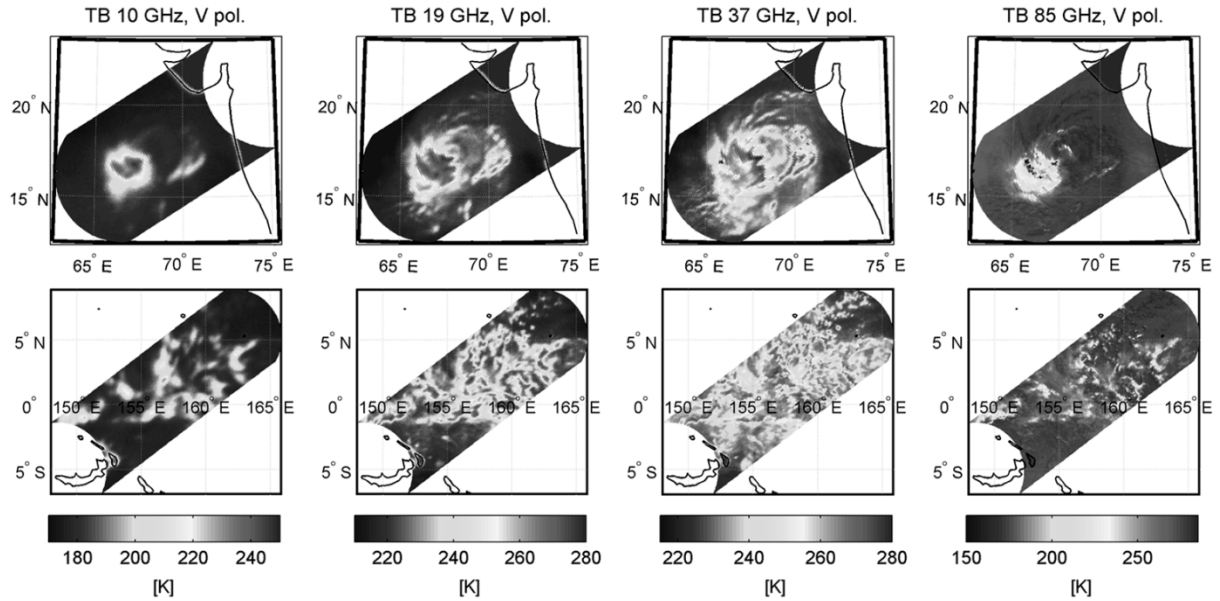


Fig. 7. TMI TBs at 10, 19, 37, and 85 GHz, all for vertical polarization, over a scattered rain system (granule 19922, upper panels) and over Cyclone 01A (granule 20112, lower panels).

TABLE VI
STATISTICS OF PR-DERIVED RAIN LWC OVER EACH
OF THE SELECTED CASE STUDIES

Case	Date	Orbit	Time (UTC)	Position (lat/lon)	PR rainy pixels	Average PR-LWC	Norm Std PR-LWC	Max PR-LWC
Tropical Storm Cimarron	11/05/2001	19883	18:28	23°N,123°E	337	0.201	0.967	1.275
	12/05/2001	19894	10:47		994	0.156	1.172	1.626
	14/05/2001	19925	10:02		1202	0.113	1.128	0.873
	14/05/2001	19928	14:53		1213	0.148	1.019	0.953
Cyclone 01A	23/05/2001	20071	16:40	17°N,70°E	868	0.270	1.483	4.574
	24/05/2001	20081	07:20		1070	0.362	1.660	5.142
	25/05/2001	20102	15:52		426	0.184	0.871	1.054
	26/05/2001	20112	06:34		656	0.412	1.568	4.582
Cyclone Adolph	26/05/2001	20119	17:12	15°N,104°E	936	0.180	1.143	1.487
	28/05/2001	20140	01:43		714	0.202	1.204	2.332
	28/05/2001	20150	16:23		669	0.168	1.145	1.583
	30/05/2001	20171	00:52		456	0.196	1.467	2.207
Scattered Rain	14/05/2001	19922	05:16	5°S,155°E	1827	0.130	1.071	1.613
Frontal System (a)	14/05/2001	19928	15:06	10°N,170°E	395	0.331	0.795	1.709
Frontal System (b)	14/05/2001	19928	15:24	25°S,130°W	553	0.135	1.045	0.764
Total					12316	0.200		5.142

A. Selected Cases

We have chosen four TRMM overpasses over three oceanic tropical systems that occurred in May 2001 [namely Cimarron in the Western Pacific (May 11–14), Cyclone 01A in the Arabian Sea (May 23–28), and Cyclone Adolph in the Eastern Equatorial Pacific (May 26–31)]. Three TRMM overpasses, each over a moderate event occurred in the same period, have also been added in order to cover a wider set of precipitating systems.

As examples, Fig. 7 shows TMI TBs for an intense event (Cyclone 01A) and for a moderate one (scattered rain system). Table VI contains the granule number and the PR-derived rain statistics for each TRMM overpass. It is interesting to note that, according to PR observations, the considered events are characterized by quite different rain LWC maxima, although the storm-averaged values are similar.

B. Comparison of BAMPR With PATER, GPROF, and PR Estimates

To perform the intercomparison, two alternative algorithms for retrieving precipitation from TMI have been considered. The first is the Gprof algorithm (TRMM level 2A12 version 5, [31]). The second is the PR-adjusted TMI estimation of rainfall algorithm (PATER) [32]. In addition, we have also taken into account the TRMM level 2A25 data product, that provides rainfall rate profiles from PR measurements according to the radar algorithm described in [33]. The PR 2A25 estimates are considered the reference and thus will be used as “truth” in the intercomparisons.

In this study, the intercomparison is made in terms of rain LWCs rather than precipitation rates to avoid the impact of different assumptions on terminal fall speed that are made for each algorithm. Since the TRMM official product for rain profile from PR is given in terms of rain rate, LWC are derived from PR measured reflectivity following the same procedure as described in [32]. Also, note that we have considered the LWC of the rain layer at 2 km height rather than that of a layer closer to the surface to minimize the number of PR pixels affected by ground clutter. Comparisons have been made at the TMI 37-GHz channel resolution. Therefore, the PR-derived LWC values have been degraded to match this resolution.

For all algorithms, estimates of hydrometeor profiles are provided already in terms of LWCs at a resolution of TMI 37 GHz; however, Gprof produces retrievals at the spatial sampling of TMI 85-GHz channels [31] so that a thinning has been performed.

Fig. 8 shows BAMPR PATER, and Gprof estimates corresponding to cases mapped in Fig. 7. The PR rain LWC retrieved at 2 km is also given to better understand their distinctive features. As for the pattern of rain estimates, BAMPR shows a high spatial variability (speckling), while PATER and Gprof are more

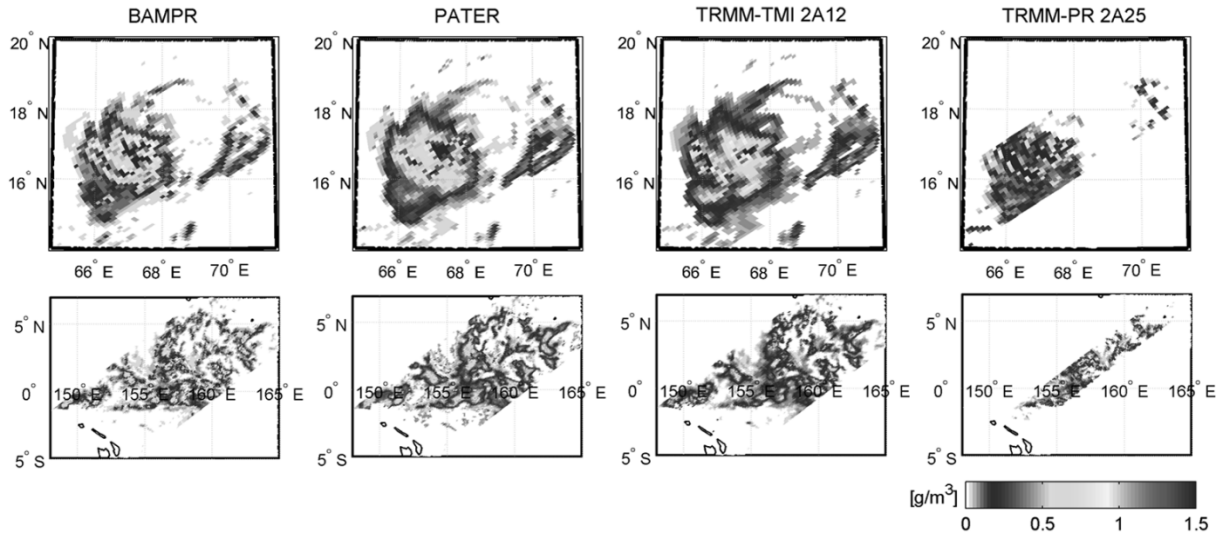


Fig. 8. (Left to right) BAMPR, PATER, Gprof, and PR (TMI averaged) rain LWC at 2 km height. Upper panels are for the scattered rain system and lower for the overpass over Cyclone 01A.

TABLE VII

(a) STATISTICS OF RAIN LWC ESTIMATED BY BAMPR, PATER, AND Gprof OVER EACH OF THE SELECTED CASE STUDIES. (b) COMPARISON OF BAMPR, PATER, AND Gprof ESTIMATES WITH THE ONES OF PR

Case	BAMPR			Gprof			PATER		
	Avera	Norm Std	Max	Avera	Norm Std	Max	Avera	Norm Std	Max
19883	0.190	1.296	1.165	0.241	0.917	1.100	0.211	1.033	0.909
19894	0.172	1.404	2.034	0.226	0.707	1.586	0.217	1.023	1.105
19925	0.118	1.462	2.204	0.203	1.216	1.546	0.141	1.461	1.512
19928	0.187	1.519	1.477	0.240	1.005	1.649	0.183	1.262	0.972
20071	0.248	1.385	2.091	0.327	1.032	2.337	0.283	1.000	1.182
20081	0.481	1.090	3.450	0.475	1.030	2.389	0.479	0.862	2.045
20102	0.101	7.344	0.426	0.194	0.592	0.620	0.154	0.749	0.471
20112	0.503	1.146	3.769	0.434	0.805	2.099	0.441	0.962	2.094
20119	0.185	1.296	1.283	0.277	1.127	2.053	0.216	1.019	1.030
20140	0.209	1.249	1.911	0.240	0.979	1.964	0.273	0.916	1.285
20150	0.181	1.248	2.254	0.239	0.850	1.667	0.243	0.934	0.981
20171	0.271	1.429	2.318	0.248	1.093	1.359	0.285	0.994	1.033
19922	0.120	1.275	2.156	0.140	0.843	1.048	0.170	0.626	1.186
19928.a	0.445	0.891	2.360	0.504	0.797	1.779	0.429	1.159	0.411
19928.b	0.093	0.750	0.713	0.127	0.675	0.564	0.092	1.312	1.812
All	0.227	-	3.769	0.262	-	2.389	0.241	-	2.094

(a)

Case	BAMPR				Gprof				PATER			
	Err Bias	Err Std	Median Abs Err	Median Err	Err Bias	Err Std	Median Abs Err	Median Err	Err Bias	Err Std	Median Abs Err	Median Err
19883	-0.011	0.247	0.079	-0.021	0.040	0.202	0.088	0.036	0.030	0.218	0.095	0.018
19894	0.016	0.172	0.039	-0.001	0.070	0.116	0.085	0.076	0.089	0.130	0.079	0.064
19925	0.065	0.185	0.038	0.015	0.090	0.164	0.043	0.042	0.049	0.130	0.048	0.010
19928	0.039	0.189	0.033	-0.003	0.091	0.139	0.056	0.052	0.058	0.123	0.042	0.018
20071	-0.022	0.360	0.068	-0.016	0.057	0.291	0.102	0.070	0.031	0.338	0.086	0.026
20081	0.012	0.489	0.098	0.020	0.011	0.396	0.100	0.072	0.014	0.544	0.111	0.078
20102	-0.083	0.140	0.052	-0.040	0.010	0.149	0.077	0.040	0.003	0.150	0.091	0.025
20112	0.091	0.544	0.126	0.030	0.022	0.488	0.157	0.099	0.011	0.495	0.180	0.105
20119	0.005	0.224	0.061	0.001	0.097	0.240	0.088	0.058	0.051	0.197	0.085	0.023
20140	0.006	0.262	0.056	-0.004	0.038	0.193	0.080	0.046	0.092	0.229	0.116	0.069
20150	0.013	0.221	0.047	-0.003	0.071	0.146	0.072	0.061	0.083	0.198	0.075	0.033
20171	0.076	0.309	0.047	0.011	0.053	0.215	0.043	0.048	0.048	0.105	0.070	0.056
19922	-0.010	0.122	0.035	-0.011	0.010	0.081	0.033	0.012	0.020	0.252	0.043	0.026
19928.a	0.011	0.355	0.136	0.026	0.017	0.288	0.127	0.094	-0.022	0.082	0.140	0.089
19928.b	-0.042	0.116	0.061	-0.020	-0.077	0.086	0.045	0.012	0.011	0.209	0.046	-0.022
All	0.026	0.284	0.051	-0.002	0.062	0.234	0.067	0.047	0.068	0.259	0.064	0.032

(b)

homogeneous. Also, these two algorithms show a general tendency to smoothen the borders of intense cells as compared to BAMPR. Similar spatial appearance characteristics are found in all the considered TRMM case studies.

A first quantitative analysis of the BAMPR, PATER, and Gprof algorithms consists of building storm-based rain statistics similar to the ones derived for PR estimates that were shown in Table VI. Table VII(a) shows that the storm-averaged rain retrieved by BAMPR is usually the lowest among the TMI algorithms, but there is no evidence that one algorithm

is closer to PR values. For each storm, rain maxima produced by BAMPR are the highest, while the ones of PATER are the lowest. The storm-based normalized standard deviation of BAMPR estimates is usually higher than for PATER and Gprof, thus confirming the more pronounced spatial variability. This was already noted by [34].

A second analysis has been made for investigating the differences between BAMPR, PATER, and Gprof estimates and those from PR. For each TRMM case and over the pixels observed by both TMI and PR and flagged as rainy by PR, the following statistical quantities have been evaluated: 1) mean; 2) median; 3) standard deviation; and 4) median of the absolute difference. As already said, the median has been considered, since it is less affected by outliers. Table VII(b) summarizes the resulting values for each algorithm. The mean and median differences are always positive for Gprof and PATER (except for frontal systems), while BAMPR overestimates in some cases and underestimates in others. As for the values they assume, BAMPR median differences are often closer to zero, followed by PATER. When considering the dispersion indicators, we note that BAMPR shows the highest standard deviation, but the lowest median absolute difference. Gprof often has the lowest standard deviation and median absolute differences intermediate to the ones of the others. PATER presents an intermediate behavior, having the lowest standard deviation in some cases. The above analysis indicates that the differences of Gprof and PATER with regard to PR are usually lower than the ones of BAMPR. This result can be related to the smooth variation observed in the pattern, while the rapid variations that BAMPR shows can lead to big mismatches with PR retrievals. However, when extreme deviations from PR estimates are omitted, BAMPR is the less distant.

Fig. 9 shows, as function of PR LWC, the normalized mean of BAMPR, PATER, and Gprof difference from PR. Here, TRMM case studies are considered all together, defining a dataset of about 17 000 coincident estimates. From their analysis it turns out that depending on the LWC value, there may be significant

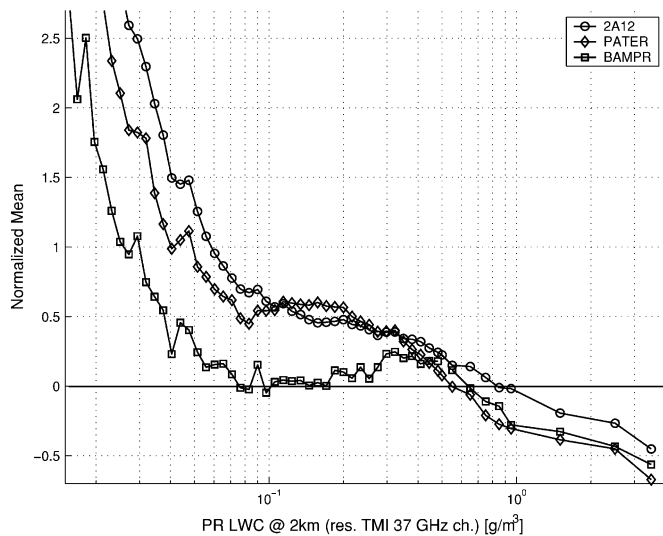


Fig. 9. Mean normalized error (with respect to PR) of the LWCs retrieved by BAMPR (line with square), PATER (line with diamond), and Gprof (line with circle), as a function of the LWC derived from the PR measurements at 1.5 km height (TMI averaged).

differences among the algorithms (as well as between them and the PR).

In particular, we note the following.

- 1) The curves have a quasi-monotonic trend for all algorithms, since they all overestimate low LWCs and underestimate the high ones.
- 2) Up to about 0.1 g/m^3 the overestimation is more evident for PATER and Gprof, which show an average error of 50% to 300% in this region. In comparison, BAMPR estimates are significantly closer to the PR ones.
- 3) Above 0.1 g/m^3 , PATER and Gprof keep overestimating (20% to 40%) up to LWCs of 0.5 and 1 g/m^3 , respectively. In contrast, between 0.1 and 1 g/m^3 BAMPR starts again increasing the overestimation reaching a maximum (about 15%) around 0.5 g/m^3 and then decreasing reaching zero at 1 g/m^3 .
- 4) As for the highest LWCs, both algorithms heavily underestimate: the retrieved values are less than half the PR ones above about 3 g/m^3 , but the BAMPR and PATER underestimation is higher. This common behavior can be attributed to the TMI spatial resolution, differently from PR, can lose some of the smallest and intense precipitating cells [10], [31].

In summary, we observe that BAMPR, PATER, and Gprof have different characteristics. This is related to different choices that each algorithm does in the various components of the retrieval scheme, although they follow the same approach (employing a CRD and performing a Bayesian inversion). The first important difference is in the CRM simulations that each of them employs (cf. Table I for BAMPR, [35] for PATER, and [2] for Gprof) as well as different assumptions on particle size distributions, particle melting and surface emission modeling. Moreover, the RT calculations are also differently performed: while a simplified 3-D geometry is employed for BAMPR and PATER, Gprof applies a one-dimensional

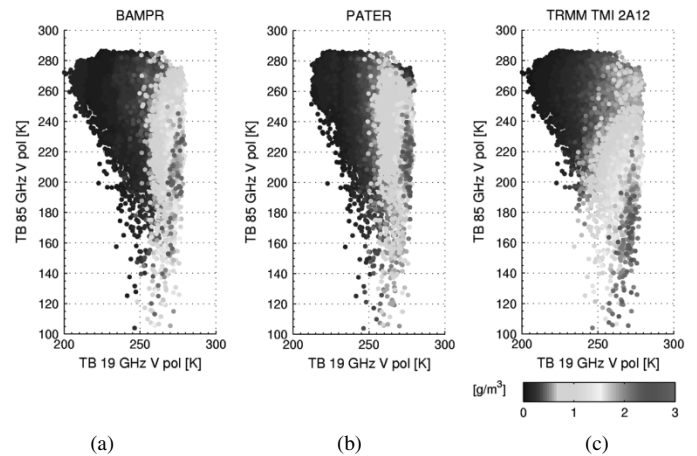


Fig. 10. Scatter plot of TBs at 85 GHz versus TBs at 19 GHz (both vertical polarization) relative to TMI measurements in the selected dataset. Grayscales in the dots refer to estimated rain LWC from (a) BAMPR, (b) PATER, and (c) Gprof.

(1-D) scheme [31]. Important dissimilarities are present in the retrieval phase as well. BAMPR directly uses TBs which are converted to principal components in case of PATER, and to *emission* and *scattering* indices in case of Gprof [31]. Finally, the error covariance matrix calculation is also different for each algorithm.

For the TRMM dataset in Table VI, Fig. 10 shows BAMPR, PATER, and Gprof rain LWC estimates plotted against the corresponding TMI TBs at 19 and 85 GHz (vertical polarization), respectively. The above listed differences in the solution of forward and inverse problem produce significant differences. Both BAMPR and PATER show a stronger gradient of LWCs with TBs at 19 GHz than with TBs at 85 GHz. Therefore, the scattering signal expressed as a reduction in TBs at 85 GHz provides little direct information on the LWC. This is possibly due to the 3-D geometry for the RT scheme that was adopted to better take into account cloud inhomogeneities, but with the drawback of an increased signal ambiguity. In the case of Gprof, LWC seems well correlated with both TBs at 19 GHz and TBs at 85 GHz. This feature can be the combined result of the introduction of the emission/scattering indices, together with the cloud fraction classification that is performed [31]. PATER shows a smaller variability of LWC with pairs of TBs at 19 and 85 GHz. This is most likely a consequence of the selection of profiles in the database using principal components for optimizing its representativeness with regard to observations. Also, the fact that the 85-GHz channels are not used in the retrievals themselves explains the weak link between observed TBs at 85 GHz and LWCs [32].

V. CONCLUSION

The characteristics of BAMPR, a Bayesian inversion method to retrieve precipitation from satellite microwave measurements, have been investigated.

An overall description of the algorithm has first been given, illustrating the CRD generation, its composition and the Bayesian formulation for the solution. The approach employed to classify the CRD has then been also exposed in detail.

In particular, two spatial pattern indicators have been introduced for the uniform/nonuniform separation. Simulation tests demonstrated that retrieval errors and estimation uncertainties are reduced over the all range of rain variability when the CRD is classified as moderate or intense, and uniform or nonuniform.

Further tests have shown the importance of an accurate evaluation of the modeling error statistics. In particular, we have noted that the retrieval is more sensitive to the modeling error at 85 GHz than to the one at 19 GHz. Results also show that estimates improve when the interchannel correlation is explicitly taken into account.

A large set of TRMM data has been finally used to evaluate rain estimates produced by BAMPR. Comparing BAMPR with PATER and Gprof, alternative TMI rainfall retrieval algorithms, we have found PATER and Gprof tend to produce higher average rain intensities while BAMPR gives higher rain maxima.

Additional differences emerge from the comparison with the rain derived from PR. BAMPR shows a better agreement with the radar at the lower rain values, while Gprof and PATER are closer to PR for higher regimes. Finally, we have shown how the diversity of each algorithm in various implementation aspects result in dissimilar TB/LWC relationships.

With the availability of new sensors flying on sun-synchronous orbits, like AMSR-E, future work will be devoted to the adaptation of the algorithm to retrieve precipitation over mid-latitude meteorological events. The implementation of a CRD calibration strategy, able to ingest information from PR in case of TRMM, or from the dual frequency precipitation radar proposed for the planned TRMM follow-on mission, is also envisaged.

APPENDIX I

THEORETICAL BACKGROUND OF BAYESIAN RETRIEVAL

Bayesian approach to precipitation retrieval has become fairly common in the remote sensing community. Indeed, the adjective “Bayesian” is very often synonymous of a statistical inversion algorithm, resembling a maximum-likelihood estimation trained by a CRD [2]. Strictly speaking, a Bayesian algorithm simply uses the Bayes theorem to obtain an optimal estimation of a set of random parameters from a given set of measurements (observables). The training of the algorithm can be carried out by either using empirical data or simulated data, depending on the relative availability and significance of the two.

The vector \mathbf{g} of cloud parameters can be treated as a random variable fully described by the probability density function (pdf) $p(\mathbf{g})$. Making the measurement \mathbf{t}_m , the conditional pdf of \mathbf{g} given \mathbf{t}_m is defined: it can be indicated as $p(\mathbf{g} | \mathbf{t}_m)$, and called *a posteriori* probability. In principle, the result of estimating \mathbf{g} through the observation \mathbf{t}_m is given by the complete pdf $p(\mathbf{g} | \mathbf{t}_m)$, although it is often convenient to represent it with only one value $\hat{\mathbf{g}}$.

Criteria to define such value are identified in the framework of the decision theory, where is assigned a “weight” $\mathbf{w}(\mathbf{g}, \hat{\mathbf{g}})$ to the couples $(\mathbf{g}, \hat{\mathbf{g}})$ of all possible values of the cloud parameters \mathbf{g} and their estimates $\hat{\mathbf{g}}$. The weight represents a measure of the quality of the estimation and is expressed as a nonnegative real

function \mathbf{W} of the two random variables \mathbf{g} and $\hat{\mathbf{g}}$. The ensemble average of the weight function is called “risk function” \mathbf{R} [36]

$$\mathbf{R} = \langle \mathbf{W}(\mathbf{g}, \hat{\mathbf{g}}) \rangle. \quad (\text{A1})$$

The risk function \mathbf{R} can be interpreted as the confidence interval of the estimate. As optimal Bayesian estimation is intended the value of \mathbf{g} minimizing \mathbf{R} . Different forms of the weight function furnish different kinds of estimation, but two are the forms leading to the most frequently used estimation criteria. The first one is the uniform weight function

$$\mathbf{W}(\mathbf{g}, \hat{\mathbf{g}}) = \begin{cases} 0, & \text{if } \mathbf{g} = \hat{\mathbf{g}} \\ 1, & \text{elsewhere.} \end{cases} \quad (\text{A2})$$

When \mathbf{W} has the expression in (A2), minimizing \mathbf{R} we obtain as optimal estimation the value of \mathbf{g} corresponding to the maximum of $p(\mathbf{g} | \mathbf{t}_m)$, i.e., its modal value

$$\hat{\mathbf{g}}_{\text{MAP}} = \text{Mode}\{\mathbf{g} | \mathbf{t}_m\}. \quad (\text{A3})$$

This represents the estimation criterion of the maximum *a posteriori* probability (MAP).

A second common form for \mathbf{W} is the quadratic one

$$\mathbf{W}(\mathbf{g}, \hat{\mathbf{g}}) = (\mathbf{g} - \hat{\mathbf{g}})^2. \quad (\text{A4})$$

In this case, it can be demonstrated that the optimal estimation is the expected value of \mathbf{g} given \mathbf{t}_m as set of measurements

$$\hat{\mathbf{g}}_{\text{MMS}} = E\{\mathbf{g} | \mathbf{t}_m\} = \int \mathbf{g} p(\mathbf{g} | \mathbf{t}_m) d\mathbf{g}. \quad (\text{A5})$$

This choice for the weight function leads to the estimation criterion of the minimum mean square (MMS).

From a numerical point of view, the implementation of (A3) imposes the search of a histogram maximum. This algorithmic aspect can be very sensitive to the sampling and the density of cloud structure parameters (and corresponding TBs) [37]. To overcome these difficulties intrinsic to the MAP solution, in BAMPR retrieval scheme we resort to the MMS criterion expressed by (A5).

Introducing the vector \mathbf{t} of simulated TB and the function $\mathbf{t}(\mathbf{g})$ that represents the adopted radiative transfer model, \mathbf{t}_m (the measurement of a real radiometer when observing \mathbf{g}) can be written as [4]

$$\mathbf{t}_m = \mathbf{t}(\mathbf{g}) + \varepsilon_t(\mathbf{g}) \quad (\text{A6})$$

where $\varepsilon_t(\mathbf{g})$ takes into account both the radiometric absolute accuracy and all other possible sources of error due to the forward modeling

$$\varepsilon_t(\mathbf{g}) = \varepsilon_{t,\text{rad}}(\mathbf{g}) + \varepsilon_{t,\text{mod}}(\mathbf{g}). \quad (\text{A7})$$

Under the previous assumptions, we have

$$p(\mathbf{t}_m | \mathbf{g}) = p[(\mathbf{t}(\mathbf{g}) + \varepsilon_t(\mathbf{g})) | \mathbf{g}] = p[\varepsilon_t(\mathbf{g})]. \quad (\text{A8})$$

Thus, according to Bayes theorem, $p(\mathbf{g} | \mathbf{t}_m)$ can be transformed in the following way:

$$p(\mathbf{g} | \mathbf{t}_m) = \frac{p(\mathbf{t}_m | \mathbf{g})p(\mathbf{g})}{p(\mathbf{t}_m)} = \frac{p[\varepsilon_t(\mathbf{g})]p(\mathbf{g})}{p(\mathbf{t}_m)} \quad (\text{A9a})$$

where $p(\mathbf{t}_m)$ is the pdf of \mathbf{t}_m .

An important aspect worth to emphasize is that, in general, Bayes' theorem represents a statistical tool to revise a given probability describing some parameters taking into account measurements. A *likelihood function* results defined every time the latter are related to the parameters under investigation according to a particular model. Equation (A9a) states that the revised probability (representing the estimation) $p(\mathbf{g} | \mathbf{t}_m)$ results as a tradeoff between the likelihood function and the given model for the parameters [in our case, $p(\mathbf{g})$]. A common approach is to take as $p(\mathbf{g})$ the occurrence of \mathbf{g} . This is reasonable when our degree of belief in the model is high enough to avoid considering any additional *virtual measurements* (e.g., climatological statistics). However, in general, when generating an estimate, the following quantity in (A9a) has to be considered and properly modeled:

$$\frac{p(\mathbf{g})}{p(\mathbf{t} = \mathbf{t}_m)} = \frac{\int p(\mathbf{t}, \mathbf{g}(\mathbf{t})) d\mathbf{t}}{\int p(\mathbf{t} = \mathbf{t}_m, \mathbf{g}(\mathbf{t})) d\mathbf{g}}. \quad (\text{A9b})$$

When as estimation value representative of $p(\mathbf{g} | \mathbf{t}_m)$ we want to consider the MMS solution $\hat{\mathbf{g}}_{\text{MMS}}$, substituting (9a) in (5) we have that it can be expressed as

$$\hat{\mathbf{g}}_{\text{MMS}} = \int \mathbf{g} \frac{p[\varepsilon_t(\mathbf{g})]p(\mathbf{g})}{p(\mathbf{t}_m)} d\mathbf{g}. \quad (\text{A10})$$

Making the further hypothesis that the error sources are independent [38], the central limit theorem lets us assume that $\varepsilon_t(\mathbf{g})$ is a random variable with Gaussian distribution

$$p[\varepsilon_t(\mathbf{g})] = \frac{1}{(2\pi)^{p/2} \sqrt{\det(\mathbf{C}_{\varepsilon_t})}} \times \exp[-0.5 (\varepsilon_t(\mathbf{g}) - \bar{\varepsilon}_t(\mathbf{g}))^T \cdot \mathbf{C}_{\varepsilon_t}^{-1}(\mathbf{g})(\varepsilon_t(\mathbf{g}) - \bar{\varepsilon}_t(\mathbf{g}))] \quad (\text{A11})$$

where $\bar{\varepsilon}_t(\mathbf{g})$ and $\mathbf{C}_{\varepsilon_t}(\mathbf{g})$ are the mean value and the covariance matrix of ε_t , respectively, while T stands for matrix transposition. Alternative forms for the measurement error model are also possible, i.e., a uniform distribution function could be more suitable in case we want that profiles that have TBs "close enough" to the measured ones could equally contribute to the estimation.

Since the two components in (A7) are supposed to be independent (thus uncorrelated), the error covariance matrix can be written as

$$\mathbf{C}_{\varepsilon_t}(\mathbf{g}) = \mathbf{C}_{\varepsilon_t, \text{rad}}(\mathbf{g}) + \mathbf{C}_{\varepsilon_t, \text{mod}}(\mathbf{g}). \quad (\text{A12})$$

If the radiometric noise has zero mean value, we also have

$$\bar{\varepsilon}_t(\mathbf{g}) = \bar{\varepsilon}_{t, \text{mod}}(\mathbf{g}). \quad (\text{A13})$$

When the dependence of ε_t from \mathbf{g} is not considered, (A11) allows to express (A10) as

$$\hat{\mathbf{g}}_{\text{MMS}} = \frac{1}{p(\mathbf{t}_m)(2\pi)^{p/2} \sqrt{\det(\mathbf{C}_{\varepsilon_t})}} \times \int \mathbf{g} \exp[-0.5(\varepsilon_t - \bar{\varepsilon}_t)^T \mathbf{C}_{\varepsilon_t}^{-1}(\varepsilon_t - \bar{\varepsilon}_t)] p(\mathbf{g}) d\mathbf{g}. \quad (\text{A14})$$

Bayesian approach allows to take into account the retrieval accuracy in a rigorous way. When \mathbf{W} has the form in (A4), it can

be proved that \mathbf{R} is equal to the conditional covariance matrix of \mathbf{g} given \mathbf{t}_m

$$\mathbf{R}_{\text{MMS}} = \mathbf{C}_{\hat{\mathbf{g}}_{\text{MMS}}} = \int (\mathbf{g} - \hat{\mathbf{g}}_{\text{MMS}})(\mathbf{g} - \hat{\mathbf{g}}_{\text{MMS}})^T p(\mathbf{g} | \mathbf{t}_m) d\mathbf{g}. \quad (\text{A15})$$

Thus, the MMS estimate has, as a confidence interval, the conditional variance of the estimate $\mathbf{C}_{\hat{\mathbf{g}}_{\text{MMS}}}$. For this reason the MMS solution can be also referred as minimum variance (MV) algorithm. Applying (A8), the previous expression can be rewritten as

$$\mathbf{C}_{\hat{\mathbf{g}}_{\text{MMS}}} = \int (\mathbf{g} - \hat{\mathbf{g}}_{\text{MMS}})(\mathbf{g} - \hat{\mathbf{g}}_{\text{MMS}})^T \frac{p[\varepsilon_t(\mathbf{g})]p(\mathbf{g})}{p(\mathbf{t}_m)} d\mathbf{g}. \quad (\text{A16})$$

The previous establishes the wanted relationship between the retrieval error $(\mathbf{g} - \hat{\mathbf{g}}_{\text{MMS}})$ and the modeling one ε_t . It is important to note that the confidence interval and the estimate itself are interconnected, since $\hat{\mathbf{g}}_{\text{MMS}}$ appears in (A16). In case the components of \mathbf{g} are uncorrelated, $\mathbf{C}_{\hat{\mathbf{g}}_{\text{MMS}}}$ becomes diagonal, with the following vector of variances

$$\sigma_{\hat{\mathbf{g}}_{\text{MMS}}}^2 = \int \mathbf{g}^2 \frac{p[\varepsilon_t(\mathbf{g})]p(\mathbf{g})}{p(\mathbf{t}_m)} d\mathbf{g} - \hat{\mathbf{g}}_{\text{MMS}}^2. \quad (\text{A17})$$

If the modeling error can be expressed as a sum of the contributions from different sources, i.e.,

$$\varepsilon_t(\mathbf{g}) = \varepsilon_{t,1}(\mathbf{g}) + \dots + \varepsilon_{t,n}(\mathbf{g}) \quad (\text{A18})$$

then it is possible to quantify the partial contribution to the uncertainty given only by a particular source introducing in (A16) only the corresponding term. The previous discussion shows how the the Bayes theorem constitutes a rigorous structure on which the retrieval approach using a CRD can be based. In addition, it is worth mentioning that the combination of different form of measurements can be easily implemented inside this methodology (e.g., see [10] for the combination with radar data).

Bayesian Formulation for the Classification: All the profiles \mathbf{g} can be clustered into n different classes C_i (with $i = 1 \dots n$). Each class contains only those profiles that we can consider "similar" according to a convenient rule. During the retrieval, the classification phase provides an estimated class \hat{C} : only the profiles contained in \hat{C} are used in the subsequent Bayesian inversion to build the final estimate. Let us indicate with \mathbf{s}_m the extended measurements (i.e., TBs and other possible quantities, like derived TB spatial pattern). The various classes C_i can be represented by means of a set of extended measurements $\bar{\mathbf{s}}(C_i)$ that we call *centroids* [39]. Choosing the MAP decision rule as suitable criterion for the classification, \hat{C} can be derived from \mathbf{s}_m as

$$\hat{C} = \text{Mode} \{ \bar{\mathbf{s}}(C_i) | \mathbf{s}_m \}. \quad (\text{A19})$$

Invoking the Bayes theorem, and making similar assumption done for the estimation itself, the conditional *a posteriori* probability can be expressed as

$$\begin{aligned} P[\bar{\mathbf{s}}(C_i) | \mathbf{s}_m] &= \frac{p(\mathbf{s}_m | \bar{\mathbf{s}}(C_i))P[\bar{\mathbf{s}}(C_i)]}{p(\mathbf{s}_m)} \\ &= \frac{p(\mathbf{s}_m - \bar{\mathbf{s}}(C_i))P[\bar{\mathbf{s}}(C_i)]}{p(\mathbf{s}_m)} \end{aligned} \quad (\text{A20a})$$

where P is the mass probability function of the centroid of the class C_i . From the previous, \hat{C} can be computed maximizing $p(\mathbf{s}_m - \bar{\mathbf{s}}(C_i))P[\bar{\mathbf{s}}(C_i)]$, since $p(\mathbf{s}_m)$ represents a common factor. If $p(\mathbf{s}_m - \bar{\mathbf{s}}(C_i))$ is considered Gaussian, thus \hat{C} minimizes the following expression:

$$(\mathbf{s}_m - \bar{\mathbf{s}}(\hat{C}))^T \mathbf{C}_{\varepsilon_s} (\mathbf{s}_m - \bar{\mathbf{s}}(\hat{C})) - \ln(P[\bar{\mathbf{s}}(\hat{C})]) \quad (\text{A20b})$$

where $\mathbf{C}_{\varepsilon_s}$ is the error covariance matrix for the variables \mathbf{s} .

For $P[\bar{\mathbf{s}}(C_i)]$, a statistics derived from external information could be used. Note that, in case P is assumed uniform and \mathbf{C}_{ε} is an identity matrix, the MAP estimate given by (A20b) reduces to the minimum distance (MD) solution [37].

APPENDIX II ROBUSTNESS TO NOISE USING A FORMULATION BY PRINCIPAL COMPONENTS

The principal components (PCs) analysis represents a statistical tool commonly used to reduce the dimensions of a set of variables without losing their intrinsic variability. Since the channels of a microwave radiometer are in the order of ten, the purpose of the reduction of the number of variables transforming TBs into PCs is to control the error related to both measured TBs (instrument noise) and to simulated ones (model uncertainties).

PCs are obtained defining a linear function that maps TBs (the original variables \mathbf{t}) into the space of PCs (the new variables \mathbf{p}). The transformation function is given by the matrix of the eigenvectors \mathbf{E}_{TB} of the TBs covariance matrix \mathbf{C}_t , i.e.,

$$\mathbf{p} = \mathbf{E}_{\text{TB}}(\mathbf{t} - \bar{\mathbf{t}}) \quad (\text{A21})$$

where $\bar{\mathbf{t}}$ is the average of the TB dataset under consideration. The covariance matrix \mathbf{C}_p of \mathbf{p} , is thus related to the one of \mathbf{t} as

$$\mathbf{C}_p = \mathbf{E}_p^T \mathbf{C}_t \mathbf{E}_p. \quad (\text{A22})$$

Let us consider the TB total error to be Gaussian with a diagonal covariance matrix $\mathbf{C}_{\varepsilon_t}$ having equal elements. In the PC space, from (A2), the error covariance matrix $\mathbf{C}_{\varepsilon_p}$ is

$$\mathbf{C}_{\varepsilon_p} = \mathbf{E}_p^T \mathbf{C}_{\varepsilon_t} \mathbf{E}_p. \quad (\text{A23})$$

According to (A22), the elements of \mathbf{C}_p along the main diagonal (i.e., the variances of the PCs) are the eigenvalues of \mathbf{C}_t . Since \mathbf{C}_p is diagonal by definition of eigenvector, the components of \mathbf{p} are uncorrelated. This property allows to perform the operation of reduction of the number of variables. Keeping only those PC components having the greater variance, a new PC vector \mathbf{p}_{red} results defined. Different objective criteria can be defined to identify the more significant PCs [40].

By using the same CRD as in Section III, Fig. 11 shows the signal-to-noise ratio over each PC components, for three different noise values. We note that the four less important components are below 0 dB; then they are completely hidden by the noise. The fourth component can be upon or below 0 dB depending on the noise value. It comes out that it should not be convenient to use them in the retrieval. To understand if the estimation really benefits from this reduction, retrieval tests internal to the CRD have been made first using TBs, then replacing them

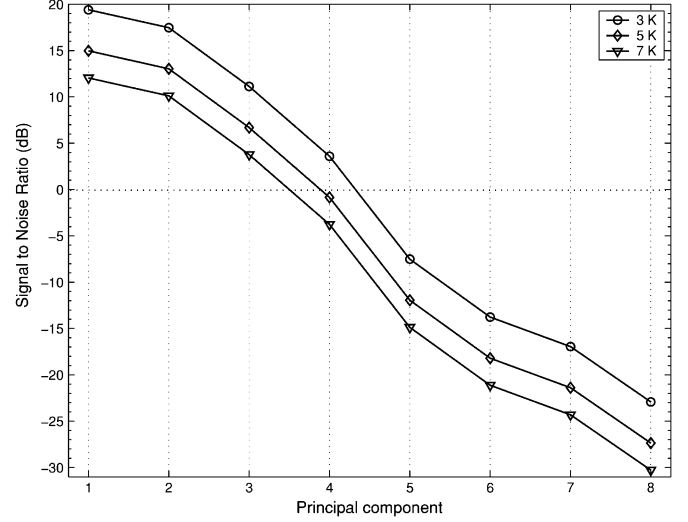


Fig. 11. Signal-to-noise ratio over each of the TB principal components. Each curve refers to the error value indicated in the legend.

TABLE VIII
TB ERROR BIAS AND STANDARD DEVIATION APPLIED TO EACH
OF THE TMI CHANNELS WITHIN THE SYNTHETIC RETRIEVAL
INDICATED BY THE TEST NUMBER

	Test 1	Test 2	Test 3	Test 4
Error Bias (K)	0	0	3	5
Error Std (K)	2	5	5	7

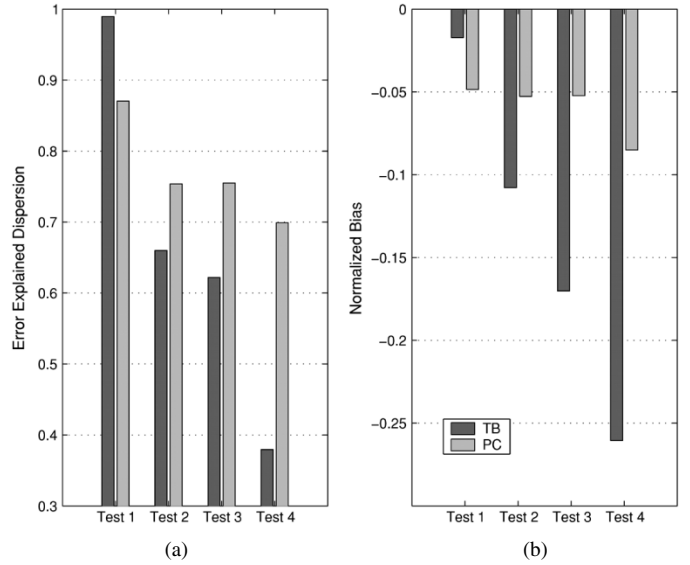


Fig. 12. (a) Estimation error dispersion and (b) error bias for the retrieval test having the error covariance matrices in Table VIII. Dark gray bars refer to tests where TB are used, while the light gray bars correspond to the ones where the first three principal components are considered.

with the three main PC components. Note that the Bayesian formulation for the inversion keeps also when the TB vector \mathbf{t} (or \mathbf{t}_m) is replaced by \mathbf{p} or with its subspace \mathbf{p}_{red} and $\mathbf{C}_{\varepsilon_t}$ is replaced by $\mathbf{C}_{\varepsilon_p}$.

Four retrieval tests have been performed, by adding each time a Gaussian noise to synthetic measurements, but using different values for the error added. Table VIII gives the values used for

the mean (bias) and for the covariance, the latter assumed diagonal with all the elements being equal. Fig. 12 shows the estimation error in each test when TBs or PCs are used. The explained median absolute retrieval error [defined as in (5)] and the median retrieval error have been again used to evaluate performances. As expected, when TBs are employed, the estimation error has a sharp increase as the noise increase, while the PC-based retrievals show a stronger immunity to noise, since both the error indicators keep almost constant.

ACKNOWLEDGMENT

The authors are very grateful to three anonymous reviewers for the helpful suggestions they provided.

REFERENCES

- [1] C. D. Kummerow *et al.*, "The status of the Tropical Rainfall Measuring Mission (TRMM) after two years in orbit," *J. Appl. Meteorol.*, vol. 39, pp. 1965–1982, 2000.
- [2] C. D. Kummerow, W. S. Olson, and L. Giglio, "A simplified scheme for obtaining precipitation and vertical hydrometeor profiles from passive microwave sensors," *IEEE Trans. Geosci. Remote Sens.*, vol. 34, no. 5, pp. 1213–1232, Sep. 1996.
- [3] N. Pierdicca, F. S. Marzano, G. D'Auria, P. Basili, P. Ciotti, and A. Mugnai, "Precipitation retrieval from spaceborne microwave radiometers using maximum a posteriori probability estimation," *IEEE Trans. Geosci. Remote Sens.*, vol. 34, no. 4, pp. 831–846, Jul. 1996.
- [4] W. S. Olson, C. D. Kummerow, G. M. Heymsfield, and L. Giglio, "A method for combined passive-active microwave retrievals of cloud and precipitation parameters," *J. Appl. Meteorol.*, vol. 35, pp. 1763–1789, 1996.
- [5] F. S. Marzano, A. Mugnai, G. Panegrossi, N. Pierdicca, E. A. Smith, and J. Turk, "Bayesian estimation of precipitating cloud parameters from combined measurements of spaceborne microwave radiometer and radar," *IEEE Trans. Geosci. Remote Sens.*, vol. 37, no. 1, pp. 596–613, Jan. 1999.
- [6] A. Mugnai, E. A. Smith, and G. J. Tripoli, "Foundations for statistical-physical precipitation retrieval from passive microwave satellite measurements. Part II: Emission source and generalized weighting function properties of a time dependent cloud-radiation model," *J. Appl. Meteorol.*, vol. 32, pp. 17–39, 1993.
- [7] G. Panegrossi, S. Dietrich, F. S. Marzano, A. Mugnai, E. A. Smith, X. Xiang, G. J. Tripoli, P. K. Wang, and J. P. V. P. Baptista, "Use of cloud model microphysics for passive microwave-based precipitation retrieval: Significance of consistency between model and measurement manifolds," *J. Atmos. Sci.*, vol. 55, pp. 1644–1673, 1998.
- [8] A. Tassa, S. Di Michele, F. S. Marzano, and A. Mugnai, "Sensitivity studies on the physical bases for TMI precipitation retrieval," presented at the 25th Eur. Geophysical Society (EGS) General Assembly, Nice, France, Apr. 25–29, 2000.
- [9] A. Tassa, S. Di Michele, F. S. Marzano, A. Mugnai, and J. P. V. P. Baptista, "Cloud-model based Bayesian technique for precipitation profile retrieval from TRMM microwave imager," *Radio Sci.*, vol. 38, p. 8074, 2003.
- [10] S. Di Michele, F. S. Marzano, A. Mugnai, A. Tassa, and J. P. V. P. Baptista, "Physically-based statistical integration of TRMM microwave measurements for precipitation profiling," *Radio Sci.*, vol. 38, p. 8072, 2003.
- [11] A. Tassa, S. Di Michele, A. Mugnai, F. S. Marzano, P. Bauer, and J. P. V. P. Baptista, "Modeling errors for passive microwave precipitation retrieval: Evaluation of a case study," *IEEE Trans. Geosci. Remote Sens.*, 2004, submitted for publication.
- [12] G. J. Tripoli, "An explicit three-dimensional nonhydrostatic numerical simulation of a tropical cyclone," *Meteorol. Atmos. Phys.*, vol. 49, pp. 229–254, 1992.
- [13] W.-K. Tao and J. Simpson, "The Goddard cumulus ensemble model. Part I: Model description," *Terrest. Atmos. Ocean. Sci.*, vol. 4, pp. 35–72, 1993.
- [14] J.-L. Redelsberger and G. Sommeria, "Three-dimensional simulation of a convective storm: Sensitivity studies on subgrid parameterization and spatial resolution," *J. Atmos. Sci.*, vol. 43, pp. 2619–2635, 1986.
- [15] H. Swann, "Sensitivity to the representation of precipitating ice in CRM simulations of deep convection," *Atmos. Res.*, vol. 48, pp. 415–435, 1998.
- [16] C. D. Kummerow, "On the accuracy of the eddington approximation for the radiative transfer in the microwave frequencies," *J. Geophys. Res.*, vol. 98, no. D10, pp. 2757–2765, 1993.
- [17] L. Roberti, J. Haferman, and C. D. Kummerow, "Microwave radiative transfer through horizontally inhomogeneous precipitating clouds," *J. Geophys. Res.*, vol. 99, no. D10, pp. 16 707–16 718, 1994.
- [18] P. Bauer, L. Schanz, and L. Roberti, "Correction of the three-dimensional effects for passive microwave remote sensing of convective clouds," *J. Appl. Meteorol.*, vol. 37, pp. 1619–1632, 1998.
- [19] R. R. Ferraro, E. A. Smith, W. Berg, and G. J. Huffman, "A screening methodology for passive microwave precipitation retrieval algorithms," *J. Atmos. Sci.*, vol. 55, pp. 1583–1600, 1998.
- [20] V. Marecal and J.-F. Mahfouf, "Four-dimensional variational assimilation of total column water in rainy areas," *Mon. Weather Rev.*, vol. 130, pp. 43–58, 2002.
- [21] I. K. Mohr, J. Famiglietti, and E. J. Zipser, "The contribution to tropical rainfall with respect to convective system type, size and intensity from 85 GHz ice-scattering signature," *J. Appl. Meteorol.*, vol. 38, pp. 596–606, 1999.
- [22] Y. Hong, C. D. Kummerow, and W. S. Olson, "Separation of convective and stratiform precipitation using microwave brightness temperatures," *J. Appl. Meteorol.*, vol. 38, pp. 1195–1213, 1999.
- [23] W. S. Olson, Y. Hong, C. D. Kummerow, and J. Turk, "A texture polarization method for estimating convective-stratiform precipitation area coverage from passive microwave radiometer data," *J. Appl. Meteorol.*, vol. 40, pp. 1577–1591, 2001.
- [24] R. M. Welch, S. K. Sengupta, and D. W. Chen, "Cloud field classification based upon high spatial resolution textural features. I. Gray level co-occurrence matrix approach," *J. Geophys. Res.*, vol. 93, no. D10, pp. 12 663–12 681, 1998.
- [25] C. Prabhakara, R. Iacovazzi, J. A. Weinman, and G. Dalu, "A TRMM microwave radiometer rain rate estimation method with convective and stratiform discrimination," *J. Meteorol. Soc. Jpn.*, vol. 78, pp. 241–258, 2000.
- [26] M. Grecu and E. N. Anagnostou, "Overland precipitation estimation from TRMM passive microwave observations," *J. Appl. Meteorol.*, vol. 40, pp. 1367–1380, 2001.
- [27] C. D. Kummerow, W. Barnes, T. Kozu, J. Shiue, and J. R. Simpson, "The Tropical Rainfall Measuring Mission sensor package," *J. Atmos. Ocean. Technol.*, vol. 15, pp. 809–817, 1998.
- [28] D. Harris and E. Foufoula-Georgiou, "Subgrid variability and stochastic downscaling of modeled clouds: Effects on radiative transfer computations for rainfall retrieval," *J. Geophys. Res.*, vol. 106, no. D10, pp. 10 349–10 362, 2000.
- [29] C. D. Kummerow, "Beamfilling errors in passive microwave rainfall retrievals," *J. Appl. Meteorol.*, vol. 37, pp. 356–370, 1998.
- [30] R. A. Houze, "Stratiform precipitation in regions of convection: A meteorological paradox?," *Bull. Amer. Meteorol. Soc.*, vol. 78, pp. 2179–2196, 1997.
- [31] C. D. Kummerow, D. B. Shin, Y. Hong, W. S. Olson, S. Yang, R. F. Adler, J. McCollum, R. Ferraro, G. Petty, and T. T. Wilheit, "The evolution of the Goddard profiling algorithm (GPROF) for rainfall estimation from passive microwave sensors," *J. Appl. Meteorol.*, vol. 40, pp. 1801–1820, 2001.
- [32] P. Bauer, P. Amayenc, C. D. Kummerow, and E. A. Smith, "Over-ocean rainfall retrieval from multisensor data of the tropical rainfall measuring mission. Part II: Algorithm implementation," *J. Atmos. Ocean. Technol.*, vol. 18, pp. 315–330, 2001.
- [33] T. Iguchi, T. Kozu, R. Meneghini, J. Awaka, and K. Okamoto, "Rain profiling algorithm for the TRMM precipitation radar," *J. Appl. Meteorol.*, vol. 39, pp. 2038–2052, 2000.
- [34] P. Bauer, J.-F. Mahfouf, W. S. Olson, F. S. Marzano, S. Di Michele, A. Tassa, and A. Mugnai, "Error analysis of TMI rainfall estimates over ocean for variational data assimilation," *Q. J. R. Meteorol. Soc.*, vol. 128, pp. 2129–2144, 2002.
- [35] P. Bauer, "Over-ocean rainfall retrieval from multi-sensor data of the tropical rainfall measuring mission. Part I: Development of inversion databases," *J. Atmos. Ocean. Technol.*, vol. 18, pp. 1315–1330, 2001.
- [36] M. Barkat, *Signal Detection and Estimation*. Boston, MA: Artech, 1991.
- [37] F. S. Marzano, S. Di Michele, A. Mugnai, and A. Tassa, "Bayesian techniques for precipitation profile retrieval from spaceborne microwave radiometric sensors," in *Proc. 5th Pacific Remote Sensing Conf. (PORSEC)*, Natl. Inst. of Oceanogr., Goa, India, Dec. 5–8, 2001, pp. 221–228, 2000.

- [38] A. C. Lorenc, "Analysis methods for numerical weather prediction," *Q. J. R. Meteorol. Soc.*, vol. 112, pp. 1177–1194, 1986.
- [39] H. C. Romesburg, *Cluster Analysis for Researchers*. Belmont, CA: Wadsworth/Lifetime, 1984.
- [40] D. S. Wilks, *Statistical Methods in Atmospheric Sciences*. London, U.K.: Academic, 1995.

Sabatino Di Michele received the laurea degree in electronic engineering and the Ph.D. degree in information and electrical engineering from the University of L'Aquila, L'Aquila, Italy, in 1997 and 2004, respectively.

Since the beginning of 1998, he has been collaborating with the Department of Electrical Engineering, University of L'Aquila, working on SSM/I applications and ground-based radiometry. In November 1998, he joined the Institute of Atmospheric Physics, CNR, Rome, Italy, to work on rainfall retrieval techniques for the Tropical Rainfall Measuring Mission (TRMM) microwave instruments. He is currently with the European Centre for Medium-range Weather Forecast (ECMWF), Reading, U.K., working on issues related to rainfall assimilation. He has been participating in various international projects (e.g., EuroTRMM, Eurainsat) concerning precipitation estimation from spaceborne microwave sensors. He is also involved in the research activity of the planned Global Precipitation Measurement Mission. His studies are mainly focused on radiative transfer modeling and on the development of new inversion procedures.

Alessandra Tassa, photograph and biography not available at the time of publication.

Alberto Mugnai, photograph and biography not available at the time of publication.



Frank Silvio Marzano (S'89–M'99–SM'03) received the laurea degree (cum laude) in electrical engineering and the Ph.D. degree in applied electromagnetics, in 1988 and 1993, respectively, both from the University of Rome "La Sapienza," Rome, Italy.

He currently teaches a course on antennas and propagation and coordinates the satellite and radar remote sensing group within the Center of Excellence CETEMPS in the Department of Electrical Engineering, University of L'Aquila, L'Aquila, Italy. In 1993, he collaborated with the Institute of

Atmospheric Physics (CNR), Rome. From 1994 until 1996, he was with the Italian Space Agency, Rome, as a Post-Doctorate Researcher. After being a Lecturer at the University of Perugia, Perugia, Italy, in 1997, he joined the Department of Electrical Engineering, University of L'Aquila. His current research interests are passive and active remote sensing of the atmosphere from ground-based, airborne, and spaceborne platforms, with a particular focus on precipitation using microwave and infrared data, development of inversion methods, radiative-transfer modeling of scattering media, and scintillation and rain-fading analysis along satellite microwave links.

Dr. Marzano received the Young Scientist Award of the XXIV General Assembly of the International Union of Radio Science in 1993. In 1998, he was the recipient of the Alan Berman Publication Award from the Naval Research Laboratory, Washington, DC. Since 2001, he is the Italian National Delegate for the European COST actions number 720 on meteorological remote sensing and number 280 on satellite communications. He is an Associate Editor for IEEE GEOSCIENCE AND REMOTE SENSING LETTERS.

Peter Bauer, photograph and biography not available at the time of publication.

José Pedro V. Poiars Baptista, photograph and biography not available at the time of publication.